Computer Physics Communications 280 (2022) 108476

Contents lists available at ScienceDirect

Computer Physics Communications

www.elsevier.com/locate/cpc

Efficacy of the symmetry-adapted basis for *ab initio* nucleon-nucleus interactions for light- and intermediate-mass nuclei ☆

A. Mercenne [a,b,*], K.D. Launey [a], T. Dytrych [c], J.E. Escher [d], S. Quaglioni [d], G.H. Sargsyan [a,d], D. Langr [e], J.P. Draayer [a]

[a] *Department of Physics and Astronomy, Louisiana State University, Baton Rouge, LA 70803, USA*
[b] *Center for Theoretical Physics, Sloane Physics Laboratory, Yale University, New Haven, CT 06520, USA*
[c] *Nuclear Physics Institute, Academy of Sciences of the Czech Republic, 25068 Řež, Czech Republic*
[d] *Lawrence Livermore National Laboratory, Livermore, CA, 94550, USA*
[e] *Department of Computer Systems, Faculty of Information Technology, Czech Technical University in Prague, Prague 16000, Czech Republic*

ARTICLE INFO

Article history:
Received 4 December 2021
Received in revised form 12 June 2022
Accepted 24 July 2022
Available online 30 July 2022

Keywords:
Nuclear physics reactions ab initio first principles symmetry

ABSTRACT

We study the efficacy of a new *ab initio* framework that combines the symmetry-adapted (SA) no-core shell-model approach with the resonating group method (RGM) for unified descriptions of nuclear structure and reactions. We obtain *ab initio* neutron-nucleus interactions for ^{4}He, ^{16}O, and ^{20}Ne targets, starting with realistic nucleon-nucleon potentials. We discuss the effect of increasing model space sizes and symmetry-based selections on the SA-RGM norm and direct potential kernels, as well as on phase shifts, which are the input to calculations of cross sections. We demonstrate the efficacy of the SA basis and its scalability with particle numbers and model space dimensions, with a view toward *ab initio* descriptions of nucleon scattering and capture reactions up through the medium-mass region.

1. Introduction

Ab initio descriptions of spherical and deformed nuclei up through the calcium region are now possible within a no-core shell-model framework, by utilizing emerging symplectic symmetry in nuclei. In particular, the symmetry-adapted no-core shell-model (SA-NCSM) [1–5] uses a physically relevant symmetry-adapted (SA) basis that can achieve significantly reduced model spaces compared to the corresponding complete ultra-large model spaces, without compromising the accuracy of results for various observables [1,6,7]. This enables the SA-NCSM to accommodate contributions from more shells and to describe heavier nuclei, such as ^{20}Ne [2], ^{21}Mg [8], ^{22}Mg [9], ^{28}Mg [10], as well as ^{32}Ne and ^{48}Ti [11,12]. The access to higher-lying shells makes the SA basis suitable for describing nuclear reactions [12], the processes that are typically studied in experiments and govern stellar evolution. Remarkable progress has been made in first-principle descriptions to scattering and nuclear reactions for light nuclei (for an overview, see [13,14]), including studies of elastic scattering [15–21], photoabsorption [22], transfer [23] and capture reactions [24], α widths [25,26] and resonant states [27], as well as thermonuclear fusion [28]. In this paper, we show that expanding the reach of *ab initio* reactions to deformed and heavier targets is now feasible with the SA basis.

Microscopic approaches to nuclear reactions take into account nucleon degrees of freedom along with their correlations within and among the reaction fragments. Coupled with realistic inter-nucleon interactions, such as the ones derived in the framework of chiral effective field theory [29–32], these approaches provide *ab initio* calculations of reaction observables. One of the earliest and very successful microscopic approaches to nuclear reactions is the resonating-group method (RGM) [33,34]. In the RGM, nucleons are organized within different groups, or clusters, "resonating" through the inter-cluster exchange of nucleons. Most importantly, the cluster system is translationally invariant, and the Pauli exclusion principle is enforced by the antisymmetrization between the different clusters. All of these features make this method particularly suitable for unified descriptions of nuclear structure and reaction observables. Following the success of the Elliott model [35,36], showing that a leading (most deformed) SU(3) shell-model configuration describes reasonably well the

☆ The review of this paper was arranged by Prof. Z. Was.

* Corresponding author.
E-mail address: alexis.mercenne@yale.edu (A. Mercenne).

https://doi.org/10.1016/j.cpc.2022.108476
0010-4655/

ground-state rotational band in intermediate-mass nuclei, the RGM has been extensively used with an SU(3) basis and its no-core shell-model extension, the symplectic Sp(3, $\mathbb{R}$) basis [37–39]. Applications of the model with Gaussian interactions have successfully calculated α and ^{8}Be cluster amplitudes, spectroscopic amplitudes for heavy-fragment clusters, and sub-Coulomb ^{12}C+^{12}C resonances [40–42]. The formalism has been extended by utilizing a mixed no-core shell-model Sp(3, $\mathbb{R}$) plus RGM cluster basis [43–45], and applied to studies of the monopole and quadrupole strengths in light nuclei [46,47], as well as the α+^{12}C cluster system [48–50].

More recently, a successful first-principle description of scattering and reactions has been realized by implementing the RGM using *ab initio* NCSM [51,52] wave functions for the clusters in a formalism known as NCSM/RGM [17,53,54] and, later, by fully combining the two approaches into the generalized *ab initio* cluster expansion of the no-core shell model with continuum (NCSMC) [55,56]. These methods, which have enabled predictions of nucleon [57,58], deuteron [59] and alpha [60] scattering off light targets, as well as polarized deuterium-tritium fusion [28] from chiral nucleon-nucleon (NN) and three-nucleon (3N) forces, are reviewed in Refs. [14,61].

In addition, the Gamow shell model coupled-channel approach combines the RGM with a continuum core-valence shell approach and allows for descriptions of nuclear reactions of heavier systems [20,62,63].

The goal of this paper is to show the efficacy of a new approach that can extend the study of *ab initio* reactions to medium mass nuclei by using the SA-NCSM approach [1,2]. The SA framework takes advantage of symmetries inherent to nuclei and of group theoretical algorithms, and reorganizes the model space into a physically relevant basis. This allows us to account for the relevant correlations within only a few dominant components and, hence, achieve manageable Hamiltonian matrix sizes. In this paper, we present a new formalism of the RGM, one that admits the use of the SA basis, and we demonstrate the capability and potential of the approach for light and intermediate-mass nuclei. The formalism of the SA-RGM framework is presented in Sec. 2, where we discuss RGM kernels computed using the SA basis. The sensitivity of the kernels on different selected model spaces and model space sizes is discussed in Sec. 3.1 for a ^{4}He target and in Sec. 3.2 for intermediate-mass ^{16}O and ^{20}Ne targets. Section 3.3 presents an analysis of the basis dimension and its scaling with model space sizes and particle numbers. Finally, Sec. 4 outlines the conclusions.

2. Theoretical framework

Traditionally, the RGM adopts microscopic cluster wave functions as basis functions to describe the motion of a system of two or more clusters (see, e.g., Refs. [53,64]). We consider two nuclear fragments, or binary-cluster nuclear reactions. For two clusters A and a, the cluster states for a channel c are defined as:

$$|\Phi^{J^\pi M}_{cr}\rangle = \{\{|(A)\mathfrak{a}_1 I_1^{\pi_1}\rangle \times |(a)\mathfrak{a}_2 I_2^{\pi_2}\rangle\}^I \times Y_\ell(\hat{r}_{A,a})\}^{J^\pi M} \times \frac{\delta(r - r_{A,a})}{r r_{A,a}}, \tag{1}$$

where the cluster system is defined for a channel $c = \{\mathfrak{a}_1, I_1^{\pi_1}, \mathfrak{a}_2, I_2^{\pi_2}, I, \ell\}$, which is labeled by the angular momentum (spin) and parity of each of the clusters and the total spin of the clusters I (the labels $\mathfrak{a}_1$ and $\mathfrak{a}_2$ denote all other quantum numbers needed to fully characterize their respective states), and the orbital momentum l. For particle laboratory coordinates $\vec{r}_i$ (used in this study), the separation distance between the center-of-mass of the two clusters is determined from $\vec{r}_{A,a} = \frac{1}{A}\sum_{i=1}^{A}\vec{r}_i - \frac{1}{a}\sum_{i=A+1}^{A+a}\vec{r}_i$. The distance r between the clusters defines the cluster states and the RGM kernels, as shown below, and as an integration variable facilitates the treatment of the inter-cluster antisymmetrization. Namely, the $A + a$ nuclear wave function is expressed in terms of the cluster states as

$$|\Psi^{J^\pi M}\rangle = \sum_c \int_r dr r^2 \frac{g_c^{J^\pi M}(r)}{r} \mathcal{A}_c |\Phi^{J^\pi M}_{cr}\rangle \ , \tag{2}$$

with unknown amplitudes $g_c^{J^\pi M}(r)$ that are determined by solving the integral Hill-Wheeler equations for a given total energy E in the $A + a$ center-of-mass frame:

$$\sum_c \int dr r^2 \left[H_{c'c}(r', r) - E N_{c'c}(r', r)\right] \frac{g_c^{J^\pi M}(r)}{r} = 0. \tag{3}$$

Here, $H_{c'c}(r', r) = \langle \Phi^{J^\pi M}_{c'r'} | \mathcal{A}_{c'} \hat{H} \mathcal{A}_c | \Phi^{J^\pi M}_{cr} \rangle$ is the Hamiltonian kernel and $N_{c'c}(r', r) = \langle \Phi^{J^\pi M}_{c'r'} | \mathcal{A}_{c'} \mathcal{A}_c | \Phi^{J^\pi M}_{cr} \rangle$ is the norm kernel, where $\mathcal{A}$ is the inter-cluster antisymmetrizer. The kernels are computed by using the microscopic wave functions of the clusters that can be obtained in the *ab initio* NCSM and SA-NCSM. Once the kernels are computed, Eq. (3) can then be solved using the microscopic R-matrix approach [65,66].

In the SA-RGM, the target nucleus of A particles is described by SA-NCSM many-body wave functions. In the SA-NCSM, the many-body basis is labeled by irreducible representations (irreps) according to the group chain [35,36]:

$$\left[\mathrm{SU}(3)_{(\lambda\,\mu)} \underset{\kappa}{\supset} \mathrm{SO}(3)_L \supset \mathrm{SO}(2)_{M_L}\right] \otimes \left[\mathrm{SU}(2)_S \supset \mathrm{SU}(1)_{M_S}\right]. \tag{4}$$

The $(\lambda\,\mu)$ quantum numbers label an SU(3) irrep and can be related to the average deformation through the established link with the well-known parameters, deformation β and triaxiality γ [67,68]. The label κ distinguishes multiple occurrences of the same orbital momentum L in the parent irrep $(\lambda\,\mu)$, and M_L is the projection. These quantum numbers define the spatial degrees of freedom, which can then be coupled to the intrinsic spin (S) to yield a good total angular momentum.

Specifically, a target state with total angular momentum and parity $I_1^{\pi_1}$ (and projection M_1) is constructed in terms of the SA basis:

$$|(A)\mathfrak{a}_1 I_1^{\pi_1} M_1\rangle = \sum_{\substack{\mathfrak{b}_1\omega_1 \\ \kappa_1 L_1 S_1}} C^{\omega_1\kappa_1 L_1 S_1 I_1}_{\mathfrak{b}_1} |\mathfrak{b}_1\omega_1\kappa_1(L_1 S_1) I_1^{\pi_1} M_1\rangle, \tag{5}$$

where the labels are defined as $\mathfrak{b} \equiv \{\ldots \omega_{\rm p}\omega_{\rm n}\rho N; S_{\rm p}S_{\rm n}\}$ and deformation $\omega \equiv (\lambda\,\mu)$ (it is understood that the coefficients C are for given π_1, which is omitted from labeling). Protons and neutrons are labeled by p and n, respectively, and S labels the intrinsic spin ("..." denotes all additional quantum numbers including $\mathfrak{a}_1$). The SU(3) outer multiplicity ρ [69] results from the coupling of the proton deformation with that of neutrons to total deformation ω_1. N labels the total harmonic oscillator (HO) excitations above the valence-shell configuration and is truncated at a maximum value ($N \leq N_{\rm max}$), which determines the model space size.

For a single-particle projectile, the SA-RGM channel basis states can thus be defined for a channel $\{\nu_1;\nu\} = \{\omega_1\kappa_1(L_1S_1);\omega\kappa(LS)\}$ [related to channel c in Eq. (13)] as:

$$|\Phi^{\nu J^\pi M}_{\nu_1 I_1;\eta}\rangle = \sum_{\mathfrak{b}_1} C^{\nu_1 I_1}_{\mathfrak{b}_1} \left\{ |\mathfrak{b}_1\omega_1 S_1\rangle \times |(\eta\,0)\frac{1}{2}\rangle \right\}^{\nu JM}, \tag{6}$$

where the SU(3) basis states for the target are coupled to the HO single-particle states of the projectile with $(\eta\,0)$ SU(3) quantum numbers and spin $\frac{1}{2}$ (we will omit the parity π from the notation throughout the paper for simplicity). We note that the SU(3) outer multiplicity associated with the coupling of ω_1 and $(\eta\,0)$ is 1, and hence, omitted from the notations. An important consequence of the use of SU(3) is that there is no dependence on the orbital momentum of the projectile, only on the shell number it occupies, η. Furthermore, the summation over $\mathfrak{b}_1$ implies that the SA-RGM basis requires only a part of the information present in the SA basis.

The SA-RGM basis is used to calculate the RGM kernels, which is the main computational task in RGM [53]. These include the norm kernel, which is the overlap between antisymmetrized non-orthogonal RGM basis states. It consists of a direct part (a Dirac delta function), which dominates at large relative distances, and an exchange part that takes into account the Pauli principle at short distances. The exchange norm kernel is related to the permutation operator $\hat{P}_{A,A+1}$ that exchanges the nucleon projectile with another nucleon within the target, thereby ensuring antisymmetrization (cf. [53]):

$$\begin{aligned} N^{\rm ex}_{c'c}(r',r) &= -\langle \Phi^{JM}_{c'r'}| \sum_{i=1}^{A} \hat{P}_{i,A+1} |\Phi^{JM}_{cr}\rangle \\ &= -A\,\langle \Phi^{JM}_{c'r'}|\,\hat{P}_{A,A+1}\,|\Phi^{JM}_{cr}\rangle \end{aligned} \tag{7}$$

The exchange norm kernel in the SA-RGM basis is thus reduced to evaluating the following (similarly, for the Hamiltonian kernels):

$$\begin{aligned} \langle \Phi^{\nu' JM}_{\nu'_1 I'_1;\eta'}|\,P_{A,A+1}\,|\Phi^{\nu JM}_{\nu_1 I_1;\eta}\rangle = \delta_{\nu'\nu} \sum_{\omega_0 S_0 \rho_0} \Pi_{S_0 S'_1} (-1)^{\eta+\eta'-\omega_0} (-1)^{S_1+\frac{1}{2}+S'} \left\{ \begin{array}{ccc} S_1 & S_0 & S'_1 \\ \frac{1}{2} & S & \frac{1}{2} \end{array} \right\} \\ \times \sqrt{\frac{\dim\omega_0}{\dim(\eta\,0)}}\, U\left[\omega_1\omega_0\omega(\eta'0);\omega'_1\rho_0 1(\eta\,0)11\right] \rho^{\rho_0\omega_0 S_0}_{\eta\eta'}\left(\nu'_1 I'_1;\nu_1 I_1\right), \end{aligned} \tag{8}$$

where $U[\ldots]$ is the SU(3) 6-$(\lambda\,\mu)$ recoupling coefficient [70], analogous to the SU(2) 6-j symbol, $\dim(\lambda\,\mu) = \frac{1}{2}(\lambda+1)(\mu+1)(\lambda+\mu+2)$, $\Pi_{j_1 j_2} = \sqrt{(2j_1+1)(2j_2+1)}$, and the SU(3) one-body density matrix elements are defined as:

$$\rho^{\rho_0\omega_0 S_0}_{\eta\eta'}\left(\nu'_1 I'_1;\nu_1 I_1\right) = \sum_{\mathfrak{b}_1\mathfrak{b}'_1} C^{\nu'_1 I'_1}_{\mathfrak{b}'_1} C^{\nu_1 I_1}_{\mathfrak{b}_1} \langle \mathfrak{b}'_1\omega'_1 S'_1|||\{a^\dagger_{(\eta\,0)\frac{1}{2}} \times \tilde{a}_{(0\,\eta')\frac{1}{2}}\}^{\omega_0 S_0}|||\mathfrak{b}_1\omega_1 S_1\rangle_{\rho_0}, \tag{9}$$

where $a^\dagger_{(\eta\,0)l m_l \frac{1}{2} m_s} \equiv a^\dagger_{\eta l m_l \frac{1}{2} m_s}$ and $a_{\eta l m_l \frac{1}{2} m_s}$ creates and annihilates, respectively, a particle of spin 1/2 in the η-th HO shell, $\tilde{a}_{(0\,\eta)l-m_l\frac{1}{2}-m_s} \equiv (-1)^{\eta+l-m_l+s-m_s} a_{\eta l m_l \frac{1}{2} m_s}$ is the annihilation SU(3) tensor operator, and $\langle\ldots|||\ldots|||\ldots\rangle$ denotes a reduced matrix element (rme) with respect to SU(3) and the spin SU(2) groups. It is notable that, as a result of the Kronecker delta function $\delta_{\nu'\nu}$ in Eq. (8), the exchange part of the norm kernel turns out to be block-diagonal in the SA-RGM basis. The reason is that the operator $\hat{P}$ is an SU(3) scalar and spin scalar, and therefore preserves deformation and spin of the composite $A+1$ system (note that it may change the ω_1 deformation of the target itself).

The matrix elements of the ρ density of Eq. (9) can be quickly computed on the fly in the SA basis. Their computation can utilize an efficacious algorithm that exploits organization of SA basis states in terms of subspaces of SU(3) irreps and the factorization of spatial SU(3) and SU(2) spin degrees of freedom [1,71], and this can be done prior to the computation of the kernels. Specifically, the essential input for the computation of $\rho^{\rho_0\omega_0 S_0}_{\eta\eta'}(\nu'_1 I'_1;\nu_1 I_1)$ is represented by the SU(3) proton-neutron rme's

$$\begin{aligned} &\langle \mathfrak{b}'_1\omega'_1 S'_1|||\{a^\dagger_{(\eta\,0)\frac{1}{2}} \times \tilde{a}_{(0\,\eta')\frac{1}{2}}\}^{\omega_0 S_0}|||\mathfrak{b}_1\omega_1 S_1\rangle_{\rho_0} \\ &\equiv \langle \left\{ \begin{array}{c} \alpha'_p\omega'_p S'_p \\ \alpha'_n\omega'_n S'_n \end{array} \right\} \rho'_1\omega'_1 S'_1|||\hat{T}^{\omega_0 S_0}_{\eta\eta'}|||\left\{ \begin{array}{c} \alpha_p\omega_p S_p \\ \alpha_n\omega_n S_n \end{array} \right\} \rho_1\omega_1 S_1\rangle_{\rho_0}, \end{aligned} \tag{10}$$

where $\hat{T}^{\omega_0 S_0}_{\eta\eta'} \equiv \{a^\dagger_{(\eta\,0)\frac{1}{2}} \times \tilde{a}_{(0\,\eta')\frac{1}{2}}\}^{\omega_0 S_0}$ and symbols $\alpha_p, \alpha'_p, \alpha_n, \alpha'_n$ schematically denote all the additional quantum numbers needed to uniquely determine proton and neutron SU(3)×SU(2) irreps. The computation of proton-neutron SU(3) rme's (10) is done by a new efficacious algorithm that exploits organization of SA basis states in terms of SU(3) equivalent irreps and also benefits from the factorization of basis states into spatial SU(3) and spin SU(2) components.

Here we briefly describe the main steps of this algorithm. Let's assume that operator $\hat{T}^{\omega_0 S_0}_{\eta\eta'}$ acts on protons (algorithm for neutron case is identical). The input for the computation of proton-neutron SU(3) rme's is then a set of non-vanishing rme's for a system of Z protons that span $0\hbar\Omega$, $1\hbar\Omega$,..., $N_{\rm max}\hbar\Omega$ model space,

$$\langle \alpha'_p \omega'_p S'_p ||| \hat{T}^{\omega_0 S_0}_{\eta\eta'} ||| \alpha_p \omega_p S_p \rangle_{\rho_p}.$$

Note that the computation of proton rme's needs to be done only once in a lifetime for a given number of Z identical nucleons and the cutoff parameter $N_{\max}$. We sort input rme's into blocks defined by rows and columns of SU(3) equivalent irreps. This allows us to maximize the reuse of computationally expensive 9-$(\lambda\,\mu)$ symbols for the computation of proton-neutron SU(3) rme's, which is executed in two main steps. In the first step, we compute the so-called proton-neutron "spinless" SU(3) rme's as

$$\begin{aligned}
&\langle \left\{ \begin{matrix} \alpha'_p \omega'_p S'_p \\ \omega_n \end{matrix} \right\} \rho'_1 \omega'_1 ||| \hat{T}^{\omega_0 S_0}_{\eta\eta'} ||| \left\{ \begin{matrix} \alpha_p \omega_p S_p \\ \omega_n \end{matrix} \right\} \rho_1 \omega_1 \rangle_{\rho_0} \\
&= \sum_{\rho_p} \begin{Bmatrix} \omega_p & \omega_0 & \omega'_p & \rho_p \\ \omega_n & (0\,0) & \omega_n & 1 \\ \omega_1 & \omega_0 & \omega'_1 & \rho_0 \\ \rho_1 & 1 & \rho'_1 & \end{Bmatrix} \langle \alpha'_p \omega'_p S'_p ||| \hat{T}^{\omega_0 S_0}_{\eta\eta'} ||| \alpha_p \omega_p S_p \rangle_{\rho_p}.
\end{aligned} \tag{11}$$

Note that "spinless" rme's do not depend on neutron spins S'_n, S_n and on total intrinsic spins S'_1 and S_1 quantum numbers. Hence, this results in a small amount of data that can be readily computed. In the second step, the resulting proton-neutron SU(3) rme's are computed by multiplying intrinsic spin dependent factor with the "spinless" rme's, namely,

$$\begin{aligned}
&\langle \left\{ \begin{matrix} \alpha'_p \omega'_p S'_p \\ \alpha'_n \omega'_n S'_n \end{matrix} \right\} \rho'_1 \omega'_1 S'_1 ||| \hat{T}^{\omega_0 S_0}_{\eta\eta'} ||| \left\{ \begin{matrix} \alpha_p \omega_p S_p \\ \alpha_n \omega_n S_n \end{matrix} \right\} \rho_1 \omega_1 S_1 \rangle_{\rho_0} \\
&= \delta_{\omega'_n \omega_n} \delta_{\alpha'_n \alpha_n} \delta_{S'_n S_n} \Pi_{S_1 S_0 S'_p S_n} \begin{Bmatrix} S_p & S_n & S_1 \\ S_0 & 0 & S_0 \\ S'_p & S_n & S'_1 \end{Bmatrix} \\
&\times \langle \left\{ \begin{matrix} \alpha'_p \omega'_p S'_p \\ \omega_n \end{matrix} \right\} \rho'_1 \omega'_1 ||| \hat{T}^{\omega_0 S_0}_{\eta\eta'} ||| \left\{ \begin{matrix} \alpha_p \omega_p S_p \\ \omega_n \end{matrix} \right\} \rho_1 \omega_1 \rangle_{\rho_0}.
\end{aligned} \tag{12}$$

The delta coefficients arise due to the spectator nature of neutrons and greatly simplify computations.

Furthermore, Eq. (8) allows the kernels to be calculated, for each J^π, through the SA-RGM channel basis of Eq. (6) that only depends on the deformation, rotation, and spin of the target ν_1 (that is, $\omega_1 \kappa_1 L_1 S_1$), and the deformation, rotation, and spin of the target-projectile system ν (that is, $\omega \kappa L S$). From this, it is clear that the SA offers two main advantages: first, calculations utilize group-theoretical algorithms that use a reduced subset of quantum numbers ν and ν_1, and second, the number of SU(3) configurations in the target wave function, we find, is a manageable number when compared to the complete model-space size. This results in a manageable number of configurations for the target-projectile system based on SU(3) and SU(2) selection rules, namely, $\omega = \omega_1 \times (\eta\,0)$ and $S = S_1 \times \frac{1}{2}$ (for further details on scalability, see Sec. 3.3).

Another advantage of the SA scheme is that the dependence on the orbital momentum ℓ is recovered in the very last step:

$$\begin{aligned}
|\Phi^{JM}_{cr}\rangle &= \sum_\eta R_{\eta\ell}(r) \sum_j \Pi_{sj} (-1)^{I_1 + J + j} \\
&\times \left\{ \begin{matrix} I_1 & \frac{1}{2} & s \\ \ell & J & j \end{matrix} \right\} \sum_{\substack{\nu \\ \nu_1}} \Pi_{L S I_1 j} \langle \omega_1 \kappa_1 L_1;\, (\eta\,0) \ell || \omega \kappa L \rangle \\
&\times \left\{ \begin{matrix} L_1 & S_1 & I_1 \\ \ell & \frac{1}{2} & j \\ L & S & J \end{matrix} \right\} |\Phi^{\nu JM}_{\nu_1 I_1; \eta}\rangle .
\end{aligned} \tag{13}$$

This wave function is then used in a microscopic R-matrix approach [65] to calculate phase shifts and cross sections.

To study the efficacy of the SA scheme, we focus on the norm and potential kernels. For the potential kernel, we consider only the part that involves the projectile and a single nucleon in the target (similarly to Ref. [21]), that is, the potential kernel of particle-rank one, denoted here as $V^{(1)}_{c'c}(r', r)$ (cf. [53]):

$$V^{(1)}_{c'c}(r', r) \equiv A \, \langle \Phi^{JM}_{c'r'} | \, \hat{V}_{A,A+1} (1 - \hat{P}_{A,A+1}) \, | \Phi^{JM}_{cr} \rangle . \tag{14}$$

Note that the exchange of two nucleons that interact with each other is part of this kernel. We do not consider the particle-rank two potential kernel that accounts for the projectile exchanging with one nucleon in the target and interacting with another nucleon (called exchange potential kernel in [53]). Since the goal of this study is to validate the use of the SA scheme against the use of complete model spaces, we expect that the particle-rank two potential kernel will benefit from advantages similar to those shown in the next section. The reason is that the main advantage stems from the reductions of the number of basis states needed to describe the target wavefunctions. Such a reduction ensures that one-body densities, along with the two-body densities that will be needed for the particle-rank two potential kernels, are computed for wavefunctions that span only a fraction of the complete model space (as discussed in Sec. 3.3).

The derivation of the potential kernel in the SA-RGM basis follows a procedure similar to that for the norm kernel:

$$\begin{aligned}
&\langle \Phi^{\nu' JM}_{\nu'_1 I'_1; \eta'} | \, (\hat{V}_{A,A+1} (1 - \hat{P}_{A,A+1})) \, | \Phi^{\nu JM}_{\nu_1 I_1; \eta} \rangle \\
&= \sum_{\substack{S_b S_a \\ S_0 S_p}} \left(\frac{\Pi_{S_p S_a}}{\Pi_{S'_0 \frac{1}{2}}} \right)^2 \frac{\Pi_{S_0}}{\Pi_{\frac{1}{2}}} \frac{1}{\Pi_{S'_1 S_a}} \, \mathrm{U} \begin{bmatrix} \frac{1}{2} & S_0 & \frac{1}{2} \\ \frac{1}{2} & S_p & \frac{1}{2} \\ S_b & S'_0 & S_a \end{bmatrix} \mathrm{U} \begin{bmatrix} S_1 & S_0 & S'_1 \\ \frac{1}{2} & S_p & \frac{1}{2} \\ S & S'_0 & S' \end{bmatrix}
\end{aligned}$$

Table 1
Model space dimension for the targets used in the present study, for $J=0^+$ in ^{4}He, ^{16}O, and ^{20}Ne, and for $J=3/2^+$ for ^{23}Mg. The complete J model spaces (all basis states) are denoted by $N_{\max}$, whereas selected model spaces are denoted as $\langle N\rangle N_{\max}$.

Nucleus	$N_{\max}$	Dimension (selected)	$N_{\max}$	Dimension (complete)
^{4}He	$\langle 6\rangle 8$	1.98×10^3	8	2.38×10^3
^{4}He	$\langle 6\rangle 10$	5.51×10^3	10	7.92×10^3
^{4}He	$\langle 6\rangle 12$	1.04×10^4	12	2.27×10^4
^{4}He	$\langle 6\rangle 14$	1.44×10^4	14	5.80×10^4
^{16}O	$\langle 0\rangle 8$	3.96×10^6	8	3.01×10^7
^{20}Ne	$\langle 2\rangle 4$	8.27×10^5	4	2.38×10^6
^{20}Ne	$\langle 2\rangle 6$	6.53×10^6	6	1.16×10^8
^{20}Ne	$\langle 2\rangle 8$	7.94×10^6	8	3.43×10^9
^{20}Ne	$\langle 2\rangle 10$	8.86×10^6	10	7.18×10^{10}
^{23}Mg	$\langle 2\rangle 4$	1.38×10^6	4	1.05×10^8
^{23}Mg	$\langle 2\rangle 6$	8.77×10^6	6	5.40×10^9
^{23}Mg	$\langle 2\rangle 8$	1.04×10^7	8	1.74×10^{11}

$$\times \sum_{\eta_b\eta_a}\sum_{\substack{\omega_b\omega_a\\ \omega_0\omega_{\rm p}}}\sum_{\substack{\rho_0'\rho_0\\ \rho'\rho_b}} \sqrt{\frac{\dim\omega_0}{\dim(\eta_b\,0)}}\frac{\dim\omega_{\rm p}\dim\omega_a}{\dim\omega_0'\dim(\eta'\,0)}\,{\rm U}\begin{bmatrix}(\eta_b\,0) & \omega_0 & (\eta_a\,0) & 1\\ (\eta\,0) & \omega_{\rm p} & (\eta'\,0) & 1\\ \omega_b & \omega_0' & \omega_a & \rho_a\\ 1 & \rho_0' & 1 & -\end{bmatrix}{\rm U}\begin{bmatrix}\omega_1 & \omega_0 & \omega_1' & \rho_0\\ (\eta\,0) & \omega_{\rm p} & (\eta'\,0) & 1\\ \omega & \omega_0' & \omega' & \rho'\\ 1 & \rho_0' & 1 & -\end{bmatrix}$$

$$\times\sqrt{1+\delta_{\eta_a\eta'}}\sqrt{1+\delta_{\eta_a\eta}}\sum_{\kappa_0'S_0'}\langle\omega\kappa L;\omega_0'\kappa_0'S_0'||\omega'\kappa'L'\rangle_{\rho'}\frac{\Pi_{L'S'}}{\Pi_{S_0'}}(-1)^{L+S_0'+S'+J}\begin{Bmatrix}L & S_0' & L'\\ S' & J & S\end{Bmatrix}$$

$$\times\langle(\eta_a0)(\eta'0);\omega_aS_a||\hat V^{\omega_0'S_0'}||(\eta_b0)(\eta0);\omega_bS_b\rangle_{\rho_0'}\rho^{\rho_0\omega_0S_0}_{\eta_a\eta_b}\left(\nu_1'I_1';\nu_1I_1\right), \tag{15}$$

where $\omega_{\rm p}$, ω_0, and ω_0' denote the SU(3) rank of the operator that transforms the initial state to the final state of the projectile, target, and the $A+1$ system, respectively.

3. Results and discussions

It is important to validate the use of the SA basis in the SA-RGM, by comparing selected model spaces with the corresponding complete $N_{\max}$, to ensure that the selection does not remove configurations relevant for the reaction processes under consideration (similar validations have been reported in Ref. [72] but for nuclear structure observables). For this, we study single-projectile scattering off the spherical ^{4}He and ^{16}O nuclei, as well as for the deformed ^{20}Ne nucleus. We present kernels that use target ground state (g.s.) wavefunctions computed with the SA basis in a complete $N_{\max}$ model space (equivalent to NCSM/RGM calculations [53]) and we compare these to the results that use wavefunctions calculated in a selected SA model space (see Table 1, including cases currently feasible only in selected model spaces). In general, SA selections are denoted as $\langle N_{\max}^{\rm C}\rangle N_{\max}$. For example, the $N_{\max}=\langle 6\rangle 14$ model space includes the complete set of excitations up to $6\hbar\Omega$ and selected excitations in the $8\hbar\Omega$ - $14\hbar\Omega$ subspaces, following a prescription detailed in Ref. [73]. This allows the mixing of all possible shapes within the complete subspaces, whereas the higher selected subspaces accommodate spatially expanded collective modes [12].

3.1. Validation of the SA scheme

We study the SA efficacy for the potential kernel of Eq. (14) for ^{4}He($0^+_{\rm g.s.}$) + n (Fig. 1), for which calculations in the complete space (no SA selection) are available up to $N_{\max}=18/19$ with other interactions ($N_{\max}=18$ denotes the model space for the target) [53]. For two NN interactions, Ref. [53] has shown that the $N_{\max}=14/15$ results are sufficient to achieve converged phase shifts for the ^{4}He($0^+_{\rm g.s.}$) + n $^2S_{1/2}$ and $^2P_{3/2}$ channels. In the present study, we use the $N_{\max}=14$ complete model space for the target, and we compare to the $N_{\max}=\langle 6\rangle 14$ model space. The ^{4}He wavefunctions in these model spaces, calculated with the JISP16 NN interactions [74], have been shown to converge for the binding energy and the g.s. root-mean-square (rms) matter radius, as well as to yield various electromagnetic sum rules [7] that agree with those calculated in the hyperspherical harmonics approach [75].

We explore the potential kernel of Eq. (14) for $P_{3/2}$ as a function of the distance between the clusters, which is used to describe the $\frac{3}{2}^-$ resonant g.s. in ^{5}He, as well as for $S_{1/2}$ for a description of the $\frac{1}{2}^+$ scattering states of ^{5}He (see Fig. 1). We find that the SA space yields results that are indistinguishable from those in the complete space. While Fig. 1 shows the comparison only for $r'=1$ fm, the results remain indistinguishable for any r'. In addition, the norm kernels exhibit the same behavior, namely, the outcomes for the SA and complete model spaces coincide. These results demonstrate that the SA wavefunctions account for the relevant correlations necessary to describe the norm and the direct component of the non-local potentials that govern the resonant ground state and low-energy scattering states in ^{5}He. Because the kernels are used as the input for calculating phase shifts, the findings show that the SA model spaces are sufficient to reproduce the corresponding $S_{1/2}$ and $P_{3/2}$ phase shifts calculated in the $N_{\max}$ complete model spaces (see Figs. 2 and 3 for the comparison of the selected model space to the complete model space). Such small differences are expected to be inconsequential. We emphasize that this comparison focuses on the effect of SA model spaces benchmarked against the corresponding complete model spaces, not on reproducing experimental phase shifts with all RGM kernels.

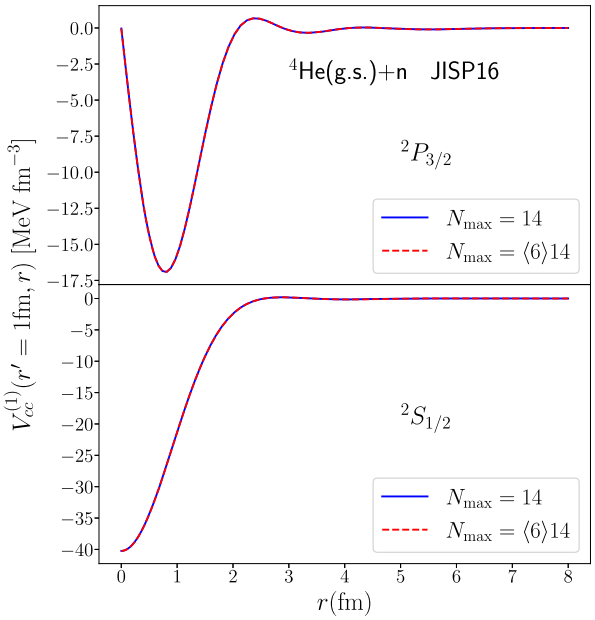

Fig. 1. Potential kernel of Eq. (15) for $^4\text{He}(0^+_{\text{g.s.}})$ + n as a function of the relative coordinate r. Calculations use the JISP16 NN interaction, for $\hbar\Omega = 25$ MeV and $\eta_{\max} = 10$, and use SA-NCSM ^{4}He wave functions in selected ($N_{\max} = \langle 6 \rangle 14$) and complete ($N_{\max} = 14$; equivalent to NCSM/RGM) model spaces. The selected space (dashed red) yields results that are indistinguishable from those in the complete space (solid blue) for both $^2P_{3/2}$ and $^2S_{1/2}$ channels. (For interpretation of the colors in the figure(s), the reader is referred to the web version of this article.)

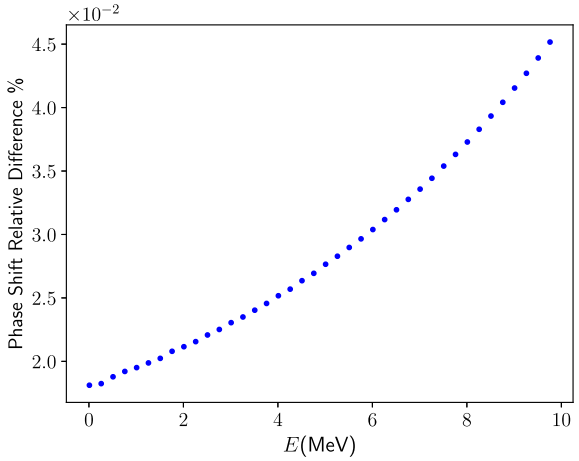

Fig. 2. Percent difference in phase shifts for the $^2S_{1/2}$ neutron scattering off ^{4}He from kernels calculated in $N_{\max}\langle 6 \rangle 14$, relative to the complete $N_{\max} = 14$ model space. Results are shown as a function of the center-of-mass projectile energy.

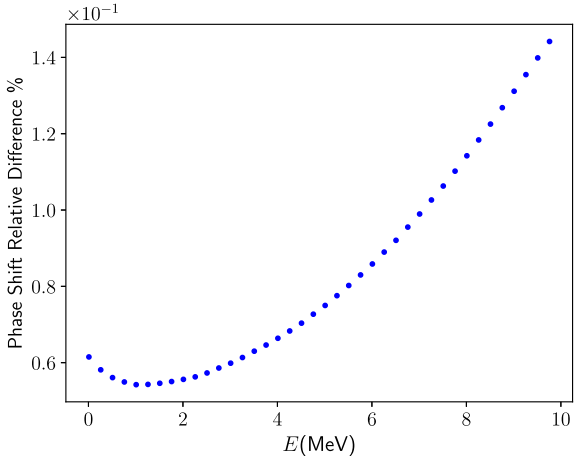

Fig. 3. Same as in Fig. 2 but for the $^2P_{3/2}$ neutron scattering off ^{4}He.

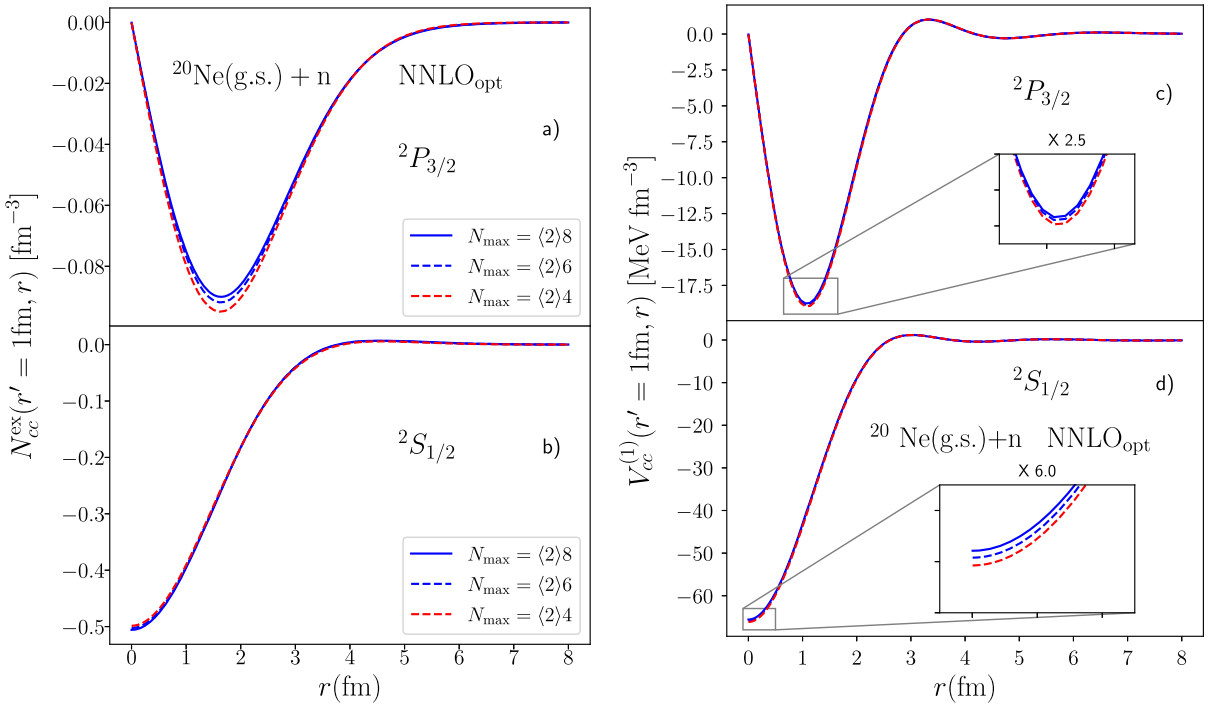

Fig. 4. (a & b) Exchange norm kernel of Eq. (8) and (c & d) potential kernel [Eqs. (14) and (15)] for ^{20}Ne($0^+_{\rm g.s.}$) + n as a function of the relative coordinate r. Calculations use the NNLO$_{\rm opt}$ NN interaction, for $\hbar\Omega = 15$ MeV and $\eta_{\rm max} = 10$, and use SA-NCSM ^{20}Ne wave functions in selected $N_{\rm max} = \langle 2\rangle 4$, $\langle 2\rangle 6$, and $\langle 2\rangle 8$ model spaces, for (a & c) $^2P_{3/2}$ and (b & d) $^2S_{1/2}$ partial waves.

3.2. Application to intermediate-mass nuclei

To illustrate the capability of the SA-RGM, we present the first *ab initio* calculations of RGM norm and leading-order potential kernels in the intermediate mass region, namely, for neutron scattering off ^{20}Ne($0^+_{\rm g.s.}$). The SA ^{20}Ne wave functions are calculated using the NNLO$_{\rm opt}$ NN interaction [76] and have been shown to reproduce observables, such as excitation energies and B(E2) strengths [2]. The NNLO$_{\rm opt}$ is used without 3N forces, which have been shown to contribute minimally to the 3- and 4-nucleon binding energies [76]. Furthermore, the NNLO$_{\rm opt}$ NN potential has been found to reproduce various observables, including the ^{4}He electric dipole polarizability [7]; the challenging analyzing power for elastic proton scattering on ^{4}He, ^{12}C, and ^{16}O [77]; along with B(E2) transition strengths for ^{21}Mg and ^{21}F [8].

As expected, the exchange norm kernel for ^{20}Ne($0^+_{\rm g.s.}$) + n manifests itself at short distances and vanishes at long distances (see Fig. 4a & b, for the case of $r' = 1$ fm). This reflects the short-range nature of the Pauli exclusion principle. We find that the change in the model space size from $N_{\rm max} = 6$ to $N_{\rm max} = 8$ has only a small effect on the exchange norm of the $P_{3/2}$ partial wave (Fig. 4a) and $S_{1/2}$ partial wave (Fig. 4b). The largest deviations are observed at short distances, where the kernels have the largest magnitude. As the model space increases, the kernels start to converge, and the exchange kernel maximum slightly increases in magnitude for $S_{1/2}$, whereas it slightly decreases for $P_{3/2}$. Note that even though the deviation seems larger for $P_{3/2}$, the magnitude of the $P_{3/2}$ exchange kernel maximum is smaller by a factor of 3.5 than that of $S_{1/2}$. Hence, these outcome indicates that the selection of dominant SU(3) components at $N_{\rm max} = 8$ (see also Fig. 3 in Ref. [2]) is sufficient to incorporate the relevant correlations needed to describe the short-range Pauli effect.

The potential kernels of Eq. (14) for ^{20}Ne($0^+_{\rm g.s.}$) + n, calculated with the NNLO$_{\rm opt}$ NN, are also studied with increasing model space sizes (see Fig. 4c & d, for $r' = 1$ fm). Similarly to the exchange norm kernel, the increase in the model space from $N_{\rm max} = 6$ to $N_{\rm max} = 8$ has a much smaller effect on this potential kernel when compared to the increase from $N_{\rm max} = 4$ to $N_{\rm max} = 6$, for both $S_{1/2}$ and $P_{1/2}$ partial waves, suggesting converging results. When compared to the potentials for ^{4}He + n of Fig. 4, the ^{20}Ne($0^+_{\rm g.s.}$) + n case shows a slightly larger deviation around the kernel maximum when varying the model space. This effect might be a result of the open-shell structure of the ground-state wave function of ^{20}Ne compared to that of ^{4}He. In addition, the small changes in these kernels result in only very little deviations in the $^2S_{1/2}$ phase shifts for the low-energy neutron scattering off ^{20}Ne($0^+_{\rm g.s.}$), with a relative difference of the order of 1-2% compared to the largest model space used (Fig. 5).

As another illustrative example, we present the potential kernel of Eq. (14) for ^{16}O($0^+_{\rm g.s.}$) + n (Fig. 6), which is feasible for no-core shell-model calculations with the importance truncation using other interactions [78]. In our study, we use the NNLO$_{\rm sat}$ [79], for which the three-nucleon (3N) forces are included in the SA-NCSM as averages [12]. Namely, in these calculations, the 3N forces are included as a mass-dependent monopole interaction [80], which has an effect on binding energies. For the ^{16}O ground-state energy, the 7-shell 3N contribution is 20.46 MeV, resulting in -127.97 MeV total energy for $N_{\rm max} = 8$ and $\hbar\Omega$=16 MeV, which agrees with the experimental value of -127.62 MeV. In this case, we compare calculations within a selected model space $N_{\rm max} = \langle 0\rangle 8$ to those in the complete $N_{\rm max} = 6$ model space. The results of the two model spaces are practically indistinguishable, despite the significantly reduced SA model space used here and the addition of SU(3) dominant configurations in the $8\hbar\Omega$ subspace. For ^{16}O, this outcome could be understood by the fact that $\sim 80\%$ of the ground state is composed of a spherical shape and low $N_{\rm max}$ model spaces are able to account for its vibrations.

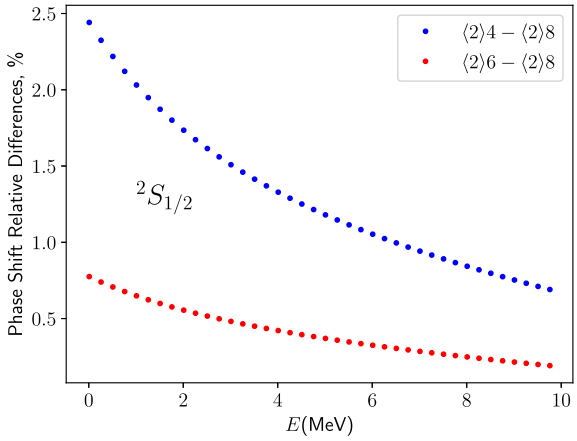

Fig. 5. Percent difference in phase shifts for the $^2S_{1/2}$ neutron scattering off ^{20}Ne from kernels calculated in $N_{\max} = \langle 2\rangle 4$ and $N_{\max} = \langle 2\rangle 6$ model spaces, relative to the phase shift from the largest model space $N_{\max} = \langle 2\rangle 8$. Results are shown as a function of the center-of-mass projectile energy.

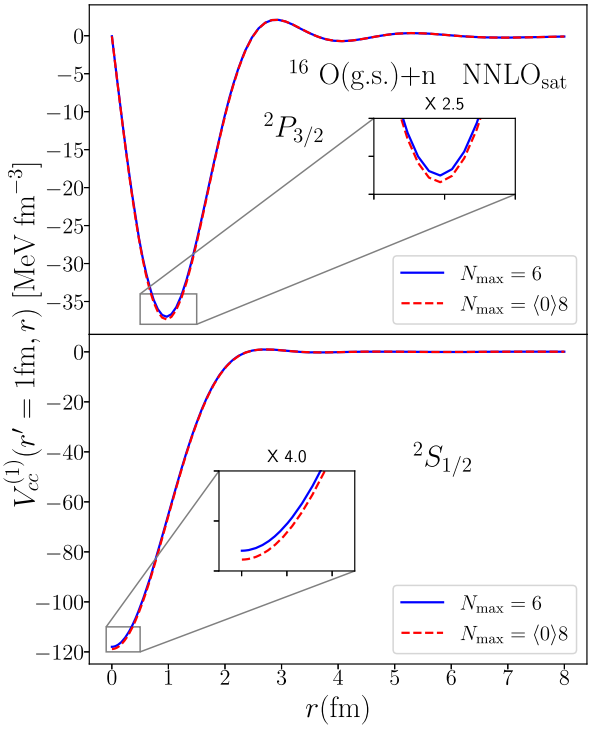

Fig. 6. Potential kernel [Eqs. (14) and (15)] for ^{16}O + n as a function of the relative coordinate r. Calculations use the NNLO$_{\rm sat}$ NN+3N interaction, for $\hbar\Omega = 16$ MeV and $\eta_{\max} = 10$, and use SA-NCSM ^{16}O wave functions in selected ($N_{\max} = \langle 0\rangle 8$) and complete ($N_{\max} = 6$) model spaces, for both $^2P_{3/2}$ and $^2S_{1/2}$ channels.

3.3. Efficacy and scalability of the SA scheme

In this section we explore the scalability of the SA-RGM calculations with increasing model space sizes and particle number. The SA-RGM channel basis (6) is used to compute the kernels of Eqs. (8) and (15). These channels are constructed from the unique $\{\nu_1\}$ quantum numbers of the target state that uses drastically reduced SA dimensions as shown in Table 1. This results in a manageable number of SA-RGM basis states, which do not require memory that scales exponentially with $N_{\max}$ as calculations in complete model spaces do. Indeed, the SA-RGM basis states remain almost constant or even decrease with $N_{\max}$, as shown in Fig. 7 for several nuclear systems.

For example, for proton- or neutron-nucleus interaction for N+^{20}Ne ($0^+_{\rm g.s.}$), there are only about 10^3-10^4 SA-RGM basis states for 7 to 13 shells, and only about $10^5 - 10^6$ for ^{23}Mg when more target states are used (with channels for $3/2^+_{\rm g.s.}$, $5/2^+$, $7/2^+$), which is still manageable (Fig. 7). Interestingly, the number of unique deformed configurations for heavier targets, such as Ne and Mg, may decrease in larger model spaces, as dominant shapes are allowed to develop, thereby reducing shape mixing. As a consequence, in such cases the SA-RGM basis can become smaller when increasing $N_{\max}$.

There is a further reduction in the number of SU(3) basis states needed for the target wave functions, as one eliminates negligible contributions identified in the target eigenfunctions. Namely, for the illustrative example of the ^{23}Mg target (Fig. 7), we show the number of the SA-RGM channels after retaining basis states that contribute with a probability amplitude $(C^{\omega_1\kappa_1 L_1 S_1}_{\mathfrak{b}_1})^2$ [see Eq. (5)] greater than a certain value ε. We find that the number of the ^{23}Mg+N SA-RGM states do not grow exponentially but remain manageable with increasing

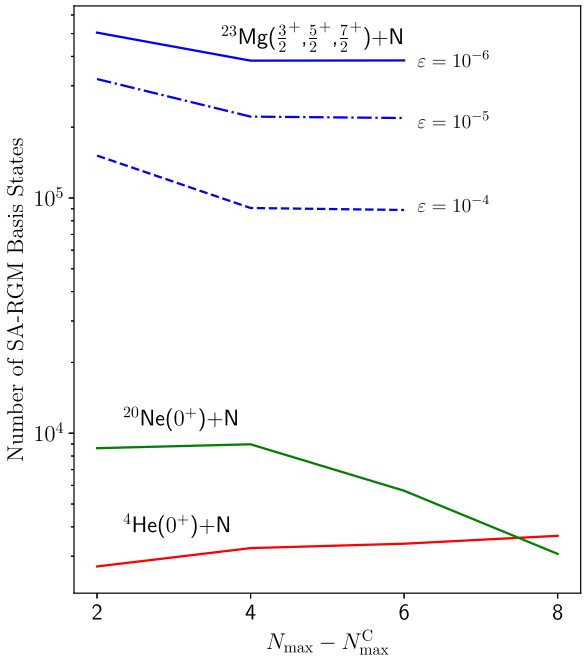

Fig. 7. Number of SA-RGM basis states as a function of the model space size $\langle N^{\mathrm{C}}_{\max}\rangle N_{\max}$ of the target. The target eigenfunctions are shown as complete (solid curves or $\varepsilon = 10^{-6}$), or reduced to the SU(3) basis states with probability amplitudes greater than ε cutoff. We use $N^{\mathrm{C}}_{\max} = 6$ for ^{4}He, and $N^{\mathrm{C}}_{\max} = 2$ for ^{20}Ne and ^{23}Mg, as well as $\eta_{\max} = 15$. The SA-NCSM calculations for ^{4}He (^{20}Ne and ^{23}Mg) use the JISP16 (NNLO$_{\mathrm{opt}}$) NN interaction and $\hbar\Omega = 25$ MeV ($\hbar\Omega = 25$ and $\hbar\Omega = 15$, respectively). The model space dimensions needed to solve for each target nucleus is given in Table 1.

$N_{\max}$ for each ε and further decreases for higher ε reduction cutoffs. We note that the $\varepsilon = 10^{-6}$ cutoff uses the ^{23}Mg basis states with a probability greater that 10^{-6} and results in no reduction. In the SA-RGM calculations, the ε cutoff for the SA selection is decreased until convergence of results is achieved.

We note that an important step for computing the kernels from the many-body wavefunctions is the calculation of the $\rho^{\rho_0\omega_0 S_0}_{\eta\eta'}$ operator of Eq. (9). Its calculation can be compared to the one-body density matrix elements, namely, they need to be calculated only once for a given set of target wavefunctions, and, as mentioned above, can utilize an efficient algorithm that exploits SU(3) SA subspaces and the factorization of spatial and spin degrees of freedom. As for the kernels, these calculations are also facilitated by the large reduction in the number of SU(3) basis states needed to describe the target wave functions, as compared to the complete $N_{\max}$ model space. These same reductions are observed for two-body densities that will be needed for the particle-rank two potential kernels.

4. Conclusions

In this paper, we have studied the efficacy of the new *ab initio* SA-RGM approach that combines the SA-NCSM and RGM frameworks. We have discussed nucleon-nucleus interactions and the use of the SA framework for ^{4}He and ^{16}O targets, as well as the intermediate-mass ^{20}Ne and ^{23}Mg targets feasible in the SA-NCSM. We have shown that the SU(3) selection of the model space has almost negligible effect on the SA-RGM norm and particle-rank one potential kernels, as well as on phase shifts used in calculations of cross sections. The results demonstrate that the reduced number of components included in the calculations are sufficient to describe single nucleon scattering in this mass region.

In addition, we have studied the scalability of the SA-RGM approach, showing its computational advantages that stem from the significantly reduced number of SU(3) basis states needed to describe the target, as well as the manageable number of the SA-RGM basis states for the target+N system with the increase in the model space size. This means that the memory resources needed for these calculations remain manageable and do not grow exponentially. The demonstrated efficacy of the SA basis and its scalability with particle numbers and model space dimensions opens the way to *ab initio* calculations up through the medium-mass region of nucleon-nucleus interactions that enter nucleon scattering and nucleon capture reactions.

Declaration of competing interest

The authors declare that they have no known competing financial interests or personal relationships that could have appeared to influence the work reported in this paper.

Data availability

Data will be made available on request.

Acknowledgements

We acknowledge useful discussions with Petr Navratil, as well as Linda Hlophe for calculating the $N_{\max} = 4$ NCSM/RGM kernel matrix elements for model benchmarks. This work was supported in part by the U.S. National Science Foundation (PHY-1913728), SURA, the Czech

Science Foundation (22-14497S), the Czech Ministry of Education, Youth and Sports under Grant No. CZ.02.1.01/0.0/0.0/16_019/0000765, and the U.S. Department of Energy Office of Science, Office of Nuclear Physics, under Work Proposals No. SCW0498 and No. SC0019521. A portion of this work was performed under the auspices of the U.S. Department of Energy by Lawrence Livermore National Laboratory under Contract No. DE-AC52-07NA27344 with support from LDRD Project No. 19-ERD-017. It benefited from high performance computational resources provided by LSU (http://www.hpc.lsu.edu), the National Energy Research Scientific Computing Center (NERSC), a U.S. Department of Energy Office of Science User Facility operated under Contract No. DE-AC02-05CH11231, as well as the Frontera computing project at the Texas Advanced Computing Center, made possible by National Science Foundation award OAC-1818253.

References

[1] K.D. Launey, T. Dytrych, J.P. Draayer, Prog. Part. Nucl. Phys. 89 (review) (2016) 101.
[2] T. Dytrych, K.D. Launey, J.P. Draayer, D.J. Rowe, J.L. Wood, G. Rosensteel, C. Bahri, D. Langr, R.B. Baker, Phys. Rev. Lett. 124 (2020) 042501.
[3] D. Langr, T. Dytrych, K.D. Launey, J.P. Draayer, Int. J. High Perform. Comput. Appl. 33 (2019) 522.
[4] D. Langr, T. Dytrych, J.P. Draayer, K.D. Launey, P. Tvrdík, Comput. Phys. Commun. 244 (2019) 442.
[5] T. Oberhuber, T. Dytrych, K.D. Launey, D. Langr, J.P. Draayer, Discrete Contin. Dyn. Syst., Ser. S 14 (2021) 1111.
[6] T. Dytrych, A.C. Hayes, K.D. Launey, J.P. Draayer, P. Maris, J.P. Vary, D. Langr, T. Oberhuber, Phys. Rev. C 91 (2015) 024326.
[7] R.B. Baker, K.D. Launey, S. Bacca, N.N. Dinur, T. Dytrych, Phys. Rev. C 102 (2020) 014320.
[8] P. Ruotsalainen, J. Henderson, G. Hackman, G.H. Sargsyan, K.D. Launey, A. Saxena, P.C. Srivastava, S.R. Stroberg, T. Grahn, J. Pakarinen, G.C. Ball, R. Julin, P.T. Greenlees, J. Smallcombe, C. Andreoiu, N. Bernier, M. Bowry, M. Buckner, R. Caballero-Folch, A. Chester, S. Cruz, L.J. Evitts, R. Frederick, A.B. Garnsworthy, M. Holl, A. Kurkjian, D. Kisliuk, K.G. Leach, E. McGee, J. Measures, D. Mücher, J. Park, F. Sarazin, J.K. Smith, D. Southall, K. Starosta, C.E. Svensson, K. Whitmore, M. Williams, C.Y. Wu, Phys. Rev. C 99 (2019) 051301.
[9] J. Henderson, et al., Phys. Lett. B 782 (2018) 468, arXiv:1709.03948 [nucl-ex].
[10] J. Williams, G.C. Ball, A. Chester, T. Domingo, A.B. Garnsworthy, G. Hackman, J. Henderson, R. Henderson, R. Krücken, A. Kumar, K.D. Launey, J. Measures, O. Paetkau, J. Park, G.H. Sargsyan, J. Smallcombe, P.C. Srivastava, K. Starosta, C.E. Svensson, K. Whitmore, M. Williams, Phys. Rev. C 100 (2019) 014322.
[11] K.D. Launey, A. Mercenne, G.H. Sargsyan, H. Shows, R.B. Baker, M.E. Miora, T. Dytrych, J.P. Draayer, in: Proceedings of the 4th International Workshop on 'State of the Art in Nuclear Cluster Physics' (SOTANCP4), May 2018, Galveston, Texas, in: AIP Conference Proceedings, vol. 2038, 2018.
[12] K.D. Launey, A. Mercenne, T. Dytrych, Annu. Rev. Nucl. Part. Sci. 71 (2021) 253.
[13] C.W. Johnson, K.D. Launey, et al., J. Phys. G 47 (2020) 23001, arXiv:1912.00451.
[14] S. Quaglioni, P. Navrátil, Nucl. Phys. News 30 (2020) 12.
[15] K. Nollett, S. Pieper, R. Wiringa, J. Carlson, G. Hale, Phys. Rev. Lett. 99 (2007) 022502.
[16] G. Hagen, D. Dean, M. Hjorth-Jensen, T. Papenbrock, Phys. Lett. B 656 (2007) 169.
[17] S. Quaglioni, P. Navrátil, Phys. Rev. Lett. 101 (2008) 092501.
[18] S. Elhatisari, D. Lee, G. Rupak, E. Epelbaum, et al., Nature 528 (2015) 111.
[19] X. Zhang, S.R. Stroberg, P. Navrátil, C. Gwak, J.A. Melendez, R.J. Furnstahl, J.D. Holt, Phys. Rev. Lett. 125 (2020) 112503.
[20] A. Mercenne, N. Michel, M. Płoszajczak, Phys. Rev. C 99 (2019) 044606.
[21] M. Burrows, R.B. Baker, C. Elster, S.P. Weppner, K.D. Launey, P. Maris, G. Popa, Phys. Rev. C 102 (2020) 034606.
[22] S. Bacca, N. Barnea, G. Hagen, M. Miorelli, G. Orlandini, T. Papenbrock, Phys. Rev. C 90 (2014) 064619.
[23] P. Navrátil, S. Quaglioni, Phys. Rev. Lett. 108 (2012) 042503.
[24] L. Girlanda, A. Kievsky, L.E. Marcucci, S. Pastore, R. Schiavilla, M. Viviani, Phys. Rev. Lett. 105 (2010) 232502.
[25] K. Kravvaris, A. Volya, Phys. Rev. Lett. 119 (2017) 062501.
[26] A.C. Dreyfuss, K.D. Launey, J.E. Escher, G.H. Sargsyan, R.B. Baker, T. Dytrych, J.P. Draayer, Phys. Rev. C 102 (2020) 044608.
[27] R. Lazauskas, E. Hiyama, J. Carbonnell, Phys. Lett. B 791 (2019) 335.
[28] G. Hupin, S. Quaglioni, P. Navrátil, Nat. Commun. 10 (2019) 351.
[29] P.F. Bedaque, U. van Kolck, Annu. Rev. Nucl. Part. Sci. 52 (2002) 339.
[30] E. Epelbaum, A. Nogga, W. Glöckle, H. Kamada, U.-G. Meißner, H. Witala, Phys. Rev. C 66 (2002) 064001.
[31] D.R. Entem, R. Machleidt, Phys. Rev. C 68 (2003) 041001.
[32] E. Epelbaum, Prog. Part. Nucl. Phys. 57 (2006) 654.
[33] K. Wildermuth, Y. Tang, A Unified Theory of the Nucleus, Vieweg, Braunschweig, 1977.
[34] Y.C. Tang, M. LeMere, D.R. Thompson, Phys. Rep. 47 (1978) 167.
[35] J.P. Elliott, Proc. R. Soc. A 245 (1958) 128.
[36] J.P. Elliott, Proc. R. Soc. A 245 (1958) 562.
[37] K.T. Hecht, Nucl. Phys. A 283 (1977) 223.
[38] K.T. Hecht, W. Zahn, Nucl. Phys. A 318 (1978) 1.
[39] K.T. Hecht, Y. Suzuki, J. Math. Phys. 24 (1982) 785.
[40] K.T. Hecht, E.J. Reske, T.H. Seligman, W. Zahn, Nucl. Phys. A 356 (1981) 146.
[41] K.T. Hecht, D. Braunschweig, Nucl. Phys. A 295 (1978) 34.
[42] Y. Suzuki, K.T. Hecht, Nucl. Phys. A 388 (1982) 102.
[43] Y. Suzuki, Nucl. Phys. A 448 (1986) 395.
[44] Y. Suzuki, K.T. Hecht, Nucl. Phys. A 455 (1986) 315.
[45] Y. Suzuki, K.T. Hecht, Prog. Theor. Phys. 77 (1987) 190.
[46] Y. Suzuki, Nucl. Phys. A 470 (1987) 119.
[47] Y. Suzuki, S. Hara, Phys. Rev. C 39 (1989) 658.
[48] Y. Suzuki, Prog. Theor. Phys. 55 (1976) 1751.
[49] Y. Suzuki, Prog. Theor. Phys. 56 (1976) 111.
[50] Y. Suzuki, R.G. Lovas, K. Yabana, K. Varga, Structure and Reactions of Exotic Nuclei, Taylor & Francis, London and New York, 2003.
[51] P. Navrátil, S. Quaglioni, I. Stetcu, B.R. Barrett, J. Phys. G, Nucl. Part. Phys. 36 (2009) 083101.
[52] B. Barrett, P. Navrátil, J. Vary, Prog. Part. Nucl. Phys. 69 (2013) 131.
[53] S. Quaglioni, P. Navrátil, Phys. Rev. C 79 (2009) 044606.
[54] G. Hupin, J. Langhammer, P. Navrátil, S. Quaglioni, A. Calci, R. Roth, Phys. Rev. C 88 (2013) 054622.
[55] S. Baroni, P. Navrátil, S. Quaglioni, Phys. Rev. Lett. 110 (2013) 022505.
[56] S. Baroni, P. Navrátil, S. Quaglioni, Phys. Rev. C 87 (2013) 034326.
[57] G. Hupin, S. Quaglioni, P. Navrátil, Phys. Rev. C 90 (2014) 061601.
[58] A. Calci, P. Navrátil, R. Roth, J. Dohet-Eraly, S. Quaglioni, G. Hupin, Phys. Rev. Lett. 117 (2016) 242501.
[59] G. Hupin, S. Quaglioni, P. Navrátil, Phys. Rev. Lett. 114 (2015) 212502.
[60] K. Kravvaris, S. Quaglioni, G. Hupin, P. Navratil, preprint, arXiv:2012.00228, 2020.
[61] P. Navrátil, S. Quaglioni, G. Hupin, C. Romero-Redondo, A. Calci, Phys. Scr. 91 (2016) 053002.
[62] Y. Jaganathen, N. Michel, M. Płoszajczak, Phys. Rev. C 89 (2014) 034624.
[63] K. Fossez, N. Michel, M. Płoszajczak, Y. Jaganathen, R.I. Betan, Phys. Rev. C 91 (2015) 034609.
[64] S. Quaglioni, C. Romero-Redondo, P. Navrátil, Phys. Rev. C 88 (2013) 034320, Erratum: Phys. Rev. C 94 (2016) 019902.

[65] P. Descouvemont, D. Baye, Rep. Prog. Phys. 73 (2010) 3.
[66] P. Descouvemont, Comput. Phys. Commun. 200 (2016) 199.
[67] O. Castaños, J.P. Draayer, Y. Leschber, Z. Phys. A 329 (1988) 33.
[68] M.T. Mustonen, C.N. Gilbreth, Y. Alhassid, G.F. Bertsch, Phys. Rev. C 98 (2018) 034317.
[69] J.P. Draayer, Y. Leschber, S.C. Park, R. Lopez, Comput. Phys. Commun. 56 (1989) 279.
[70] J.P. Draayer, Y. Akiyama, J. Math. Phys. 14 (1973) 1904.
[71] T. Dytrych, K.D. Sviratcheva, C. Bahri, J.P. Draayer, J.P. Vary, Phys. Rev. Lett. 98 (2007) 162503.
[72] T. Dytrych, P. Maris, K.D. Launey, J.P. Draayer, J.P. Vary, M. Caprio, D. Langr, U. Catalyurek, M. Sosonkina, Comput. Phys. Commun. 207 (2016) 202.
[73] K.D. Launey, T. Dytrych, G.H. Sargsyan, R.B. Baker, J.P. Draayer, Eur. Phys. J. Spec. Top. 229 (2020) 2429.
[74] A. Shirokov, J. Vary, A. Mazur, T. Weber, Phys. Lett. B 644 (2007) 33.
[75] S. Bacca, N. Barnea, G. Hagen, G. Orlandini, T. Papenbrock, Phys. Rev. Lett. 111 (2013) 122502.
[76] A. Ekström, G. Baardsen, C. Forssén, G. Hagen, M. Hjorth-Jensen, G.R. Jansen, R. Machleidt, W. Nazarewicz, et al., Phys. Rev. Lett. 110 (2013) 192502.
[77] M. Burrows, C. Elster, S.P. Weppner, K.D. Launey, P. Maris, A. Nogga, G. Popa, Phys. Rev. C 99 (2019) 044603.
[78] P. Navrátil, R. Roth, S. Quaglioni, Phys. Rev. C 82 (2010) 034609.
[79] A. Ekström, G.R. Jansen, K.A. Wendt, G. Hagen, T. Papenbrock, B.D. Carlsson, C. Forssén, M. Hjorth-Jensen, P. Navrátil, W. Nazarewicz, Phys. Rev. C 91 (2015) 051301.
[80] K.D. Launey, T. Dytrych, J.P. Draayer, Phys. Rev. C 84 (2012) 044003.